MATERIALS CHEMISTRY
FRONTIERS

RESEARCH ARTICLE

View Article Online
View Journal | View Issue

Cite this: *Mater. Chem. Front.*, 2019, **3**, 1823

A novel family of AIE-active *meso*-2-ketopyrrolyl BODIPYs: bright solid-state red fluorescence, morphological properties and application as viscosimeters in live cells†

Changjiang Yu,‡[abc] Zhenlong Huang,‡[d] Wei Gu,[a] Qinghua Wu,[a] Erhong Hao,*[a] Yi Xiao,*[d] Lijuan Jiao*[a] and Wai-Yeung Wong*[b]

Received 13th March 2019,
Accepted 25th June 2019

DOI: 10.1039/c9qm00154a

rsc.li/frontiers-materials

Fluorescent probes towards viscosity determination can be used to report on variations in local molecular viscosity and have become valuable tools for the study of intracellular microenvironments. Herein, we develop a family of remarkable *meso*-2-ketopyrrolyl-derived BODIPY rotors and report a new strategy for building them *via* simple condensation reactions between oxalyl chloride and substituted pyrroles. They are well characterized by NMR, HRMS, crystal structure, spectroscopic and morphological studies. These uncommon *meso*-2-ketopyrrolyl-derived BODIPYs are weakly fluorescent in their organic solutions but exhibit bright solid-state red fluorescence from 620 to 661 nm with a maximum fluorescence quantum yield of 25%. All of them also exhibit notable aggregation-induced emission (AIE)-active features. Interestingly, the formed nanoaggregates were observed to exhibit morphological distinctions owing to different substituents. The fluorescence enhancement towards the increased viscosity of the environment might be mainly attributed to the restriction of their intramolecular rotations of the *meso*-ketopyrrolyl groups. More interestingly, the increase in the fluorescence lifetime of these representative rotors appears to perfectly correlate with the increase in the viscosity of the media, and they have been used as viscosimeters for real-time quantitative determination of the variation of the intracellular viscosity in live cells. The easy synthetic strategy and real-time quantitative determination of the variation pave a new way for creating fluorescent molecular rotor materials.

1. Introduction

Intracellular micro-viscosity has a very important role in the study of multifarious signal transportation and cellular processes such as reticulophagy and division/death of cells.[1] Among various strategies for measuring viscosity directly, membrane permeable fluorescent molecular rotors (FMRs) that are sensitive to the viscosity of the surrounding microenvironments have been regarded as a class of the most successful probes for intracellular viscosity.[2,3] The developed rotors suitable for fluorescence intensity or fluorescence lifetime imaging techniques usually undergo molecular rotation and further effectively dissipate their excitation energies. The corresponding fluorescence signals could be used to directly report the variations in local molecular viscosity, especially for some abnormal changes, which are closely associated with many diseases and pathologies including diabetes and Alzheimer's disease.[4]

Recently, some elegant FMRs based on fluorescent BODIPY (boron dipyrromethene)[5] segments have been developed due to their high fluorescence quantum yields and the high rotational ability of the substituents at the *meso*-position, giving a linear correlation between their fluorescence lifetime and viscosity, and widely applied as viscosity sensors in intracellular microenvironments in fluorescence lifetime imaging microscopy (FLIM) techniques.[1d,6–11] However, most of the recently developed BODIPY-based FMRs almost have similar cores of *meso*-phenyl substituted BODIPYs.[1b,6–10] The efficient strategy for these BODIPY FMRs is based on the rotation of the *meso*-phenyl

---

[a] *The Key Laboratory of Functional Molecular Solids, Ministry of Education, Anhui Laboratory of Molecule-Based Materials (State Key Laboratory Cultivation Base), School of Chemistry and Materials Science, Anhui Normal University, Wuhu, China. E-mail: haoehong@ahnu.edu.cn, jiao421@ahnu.edu.cn*

[b] *Department of Applied Biology and Chemical Technology, The Hong Kong Polytechnic University, Hung Hom, Kowloon, Hong Kong, China. E-mail: wai-yeung.wong@polyu.edu.hk*

[c] *State Key Laboratory of Coordination Chemistry, Nanjing University, Nanjing 210093, China*

[d] *State Key Laboratory of Fine Chemicals, Dalian University of Technology, 2 Linggong Road, Dalian 116024, China. E-mail: xiaoyi@dlut.edu.cn*

† Electronic supplementary information (ESI) available: Fig. S1–S31 and Tables S1–S4. CCDC 1541729, 1541728 and 1901461 for **1a–c**. For ESI and crystallographic data in CIF or other electronic format see DOI: 10.1039/c9qm00154a

‡ C. Y. and Z. H. contributed equally.

group around a C–C single bond, which causes a non-radiative decay in the excited state in non-viscous media.[9] An increase of viscosity makes it more difficult to rotate the *meso*-phenyl group. This inhibits the non-radiative decay process and brings an increase of fluorescence lifetime. Using this strategy, one group of us previously developed a BODIPY-based FMR for high temporal and spatial determination of lysosomal viscosity in living cells through FLIM.[10] Different from conventional BODIPY-based FMRs, only one example of BODIPY **B** distorted from internal steric hindrance between the 1,7-dimethyl group and the *meso*-CHO was found as an impactful viscosimeter in 2014 by Fan and Peng.[11] Nevertheless, despite some advantages, BODIPY dyes exhibit some drawbacks such as low fluorescence quantum yields in the solid state and relatively complicated syntheses. Based on the above studies, we rationalized that a less bulky group such as 2-ketopyrrolyl (than phenyl) at the *meso*-position of a BODIPY at the same time together with the 1,7-dimethyl group may allow its rotation in non-viscous media. This kind of BODIPY dye might show bright solid-state emission and provide an alternative strategy for synthesizing novel unconventional and efficient viscosity probes.

Herein, we develop a new strategy for building uncommon *meso*-2-ketopyrrolyl BODIPY derivatives containing the 1,7-dimethyl group (Fig. 1), which exhibit great performance comparable or even superior to those of conventional BODIPY-based FMRs. Firstly, the easy synthetic method of the two *meso*-2-ketopyrrole derived BODIPYs has been reported for the first time *via* simple condensation between commercial oxalyl chloride and pyrrole derivatives. Secondly, these rotors unexpectedly showed notable aggregation-induced emission (AIE) features and bright red fluorescence in the solid state. Thirdly, their fluorescence intensity and lifetime were observed to perfectly correlate with the viscosity of the medium. The real-time determination of the variation of the viscosity in live cells by using FLIM has been successfully demonstrated, which qualifies them as a novel class of BODIPY-derived molecular rotors.

2. Results and discussion

2.1 Synthesis and characterization

Initially, the desired *meso*-2-ketopyrrolyl BODIPY **1a** was synthesized by the condensation of oxalyl chloride with a stoichiometric amount of 2,4-dimethyl-3-ethylpyrrole, and a subsequent BF_2 complexation under refluxing conditions (Scheme 1), which was confirmed by single crystal X-ray crystallography. Interestingly, similar condensation of oxalyl chloride with 2 eq. of 2,4-dimethyl-3-ethylpyrrole at room temperature by Akkaya and coworkers gave unexpected two difluoroboron chelated oxalyl-tethered pyrroles.[12] The reaction conditions were then optimized and we found that 3.5 eq. of 2,4-dimethyl-3-ethylpyrrole was enough for obtaining the targeted *meso*-2-ketopyrrolyl derived BODIPY **1a**. Under the optimized conditions, the desired *meso*-2-ketopyrrolyl substituted BODIPYs **1a** and **1b** were synthesized from the corresponding pyrroles in one pot in 18% and 23% yields, respectively. Dipyrrolyldiketones **2a–b** prepared from oxalyl chloride and substituted pyrroles[13] were then found to succeed in condensing with another pyrrole molecule under $BF_3{\cdot}OEt_2$, respectively, followed by the complexation with $BF_3{\cdot}OEt_2$ in the presence of triethylamine (Scheme 1), from which the targeted *meso*-2-ketopyrrolyl BODIPYs **1a–d** were prepared in 32–45% yields. The chemical shifts δ of *meso*-uncoordinated pyrrolic β-H at 5.84 ppm for **1b** and **1d**, respectively, revealed much higher fields than those of coordinated pyrrolic β-H. These *meso*-2-ketopyrrolyl BODIPYs were well characterized by ^1H and ^{13}C NMR and HRMS. Their structures were further confirmed by single crystal X-ray crystallography. Several *meso*-ester BODIPYs have been reported;[14] however, the synthesis of *meso*-ketone derived BODIPYs has not been previously developed. Our method developed here provides a facile access to these novel BODIPYs of this kind for the first time. More interestingly, Bae and Kim demonstrated a fluorogenic J-aggregating *meso*-ester BODIPY recently, which could selectively monitor and image eosinophil peroxidase activity.[14e]

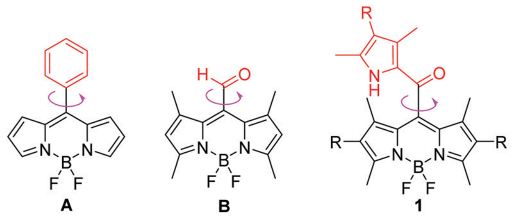

Fig. 1 The chemical structures of FMRs: conventional *meso*-phenyl derived BODIPY **A**, *meso*-aldehyde derived BODIPY **B** and our designed *meso*-2-ketopyrrolyl BODIPYs **1** in this contribution.

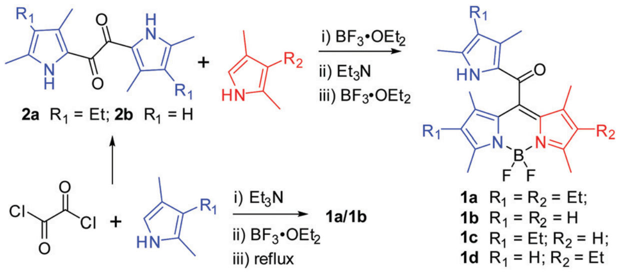

Scheme 1 Syntheses of *meso*-2-ketopyrrolyl BODIPYs **1a–d**.

2.2 X-ray crystallography

The crystal structure plots for the *meso*-2-ketopyrrolyl derived BODIPYs **1a–c** are given in Fig. 2 and Fig. S1–S3 in the ESI† and the crystal data are listed in Tables S1 and S2 (ESI†). They all belong to the monoclinic space group *C*2/*c* and their boron atoms show a tetrahedral structure. The average B–N distances for **1a–b** are almost the same (1.54 Å for **1a** and 1.55 Å for **1b**), supporting their symmetrical structures. In sharp contrast to them, the average B–N distances of **1c** are 1.53 and 1.55 Å, confirming the unsymmetrical structures of **1c** and **1d**. What deserves to be mentioned is that the dipyrrin cores of these novel *meso*-2-ketopyrrolyl BODIPYs are planar, which is similar to previously reported BF_2 complexes,[15] and the dihedral angles defined by two coordinated pyrrolic rings are 5.0°, 8.8° and 1.5° (Table S1, ESI†) for **1a–c**, respectively. This indicates that the

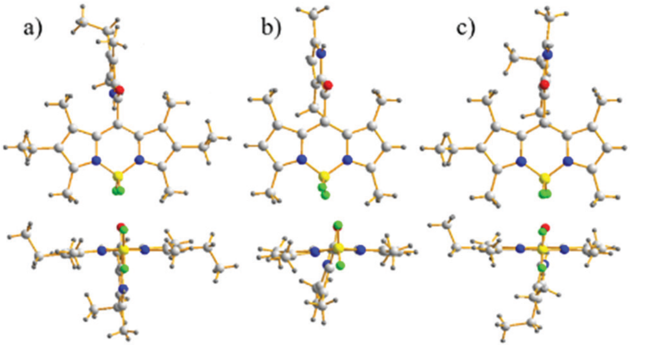

Fig. 2 Front and top views of the X-ray structures for *meso*-2-ketopyrrolyl BODIPYs **1a–c**. C, light gray; H, gray; N, blue; F, bright green; B, yellow; O, red.

installation of a steric *meso*-2-ketopyrrolyl substituent into the BODIPY core causes negligible structural distortion of the planarity of the BODIPY core structure. The carbonyl group as a linker avoided internal steric hindrance between the BODIPY core and the uncoordinated pyrrole ring at the *meso*-position. The results are quite different from the "distorted BODIPY" **B**, although they both have the same 1,7-dimethyl group and the carbonyl group. The carbonyl group and the uncoordinated pyrrole ring in their crystals are coplanar. In addition, the dihedral angles defined by the *meso*-2-ketopyrrolyl moiety and the BODIPY core are 88.8°, 72.9° and 81.4°, respectively, for **1a–c** (Table S1, ESI†), which are almost vertical.

2.3 Photophysical studies

The absorption and emission spectra (Fig. 3 and Fig. S4–S9, ESI†) of these *meso*-2-ketopyrrolyl BODIPYs **1a–d** were measured in various common organic solvents with different polarities such as cyclohexane, toluene, dichloromethane, tetrahydrofuran, acetonitrile and methanol (Table S3, ESI†). They all exhibit a strong absorption band in the 450–550 nm region. For example, **1a** exhibits an intense absorption band centred at 534 nm with a high extinction coefficient of $4.81 \times 10^4\ \mathrm{M}^{-1}\ \mathrm{cm}^{-1}$ (Fig. 3a and Fig. S4, Table S3, ESI†). With respect to **1b** in dichloromethane, obvious bathochromic shifts were observed for **1a** and **1c** (Fig. 3a and Fig. S4 and S8, ESI†). It is worth mentioning that **1c** and **1d** with the same unsymmetrical BODIPY core exhibit almost the same absorption and emission (Fig. S8 and S9 and Table S3, ESI†). The results indicate that the enhancement of the intramolecular charge transfer (ICT) effect of alkyl substituents on the coordinated pyrrole ring might mainly contribute to the observed bathochromic shifts. Besides, these *meso*-2-ketopyrrolyl BODIPYs exhibit relatively large Stokes shifts ranging from 653 to 986 cm^{-1}. In addition, no significant variations of the absorption and emission maxima were observed with the variation of the polarity of the organic solvents for them although a slight variation of the fluorescence intensity was observed (Table S3, ESI†).

In comparison with most BODIPY dyes,[15] most of these *meso*-2-ketopyrrolyl BODIPYs are poorly emissive in organic solvents except for **1a**, which exhibit relatively much higher fluorescence quantum yields (ϕ) of 0.10–0.21 (Table S3, ESI†).

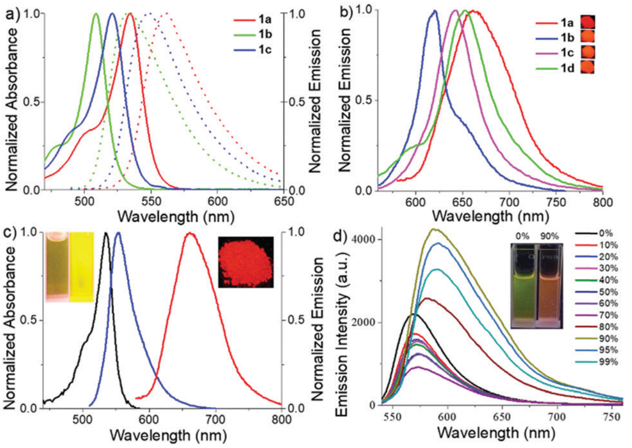

Fig. 3 (a) Overlaid normalized absorption and emission spectra of **1a–c** in dichloromethane, excited at 480 nm for **1a** and 460 nm for **1b and c**. (b) Normalized emission spectra of **1a–d** in the powder state, excited at 550 nm for **1a** and 500 nm for **1b–d**. Photographs of their powders under 365 nm UV lamp irradiation. (c) Normalized absorption (black) and emission (blue) spectra in glycerol, and the emission spectrum in the powder state (red) of **1a**. Photographs of the samples in daylight and under 365 nm UV lamp irradiation. (d) Emission spectra of **1a** in acetonitrile/water with different water fractions, excited at 500 nm.

For example, the fluorescence quantum yields were evaluated to be 0.03 and 0.01, respectively, for **1b** and **1c** in acetonitrile. The possible rotations of the *meso*-2-ketopyrrolyl group might result in the internal conversion through a non-radiative process. As expected, **1a** and **1b** indeed show bright fluorescence emission in glycerol, with fluorescence quantum yields of 0.43 and 0.15, respectively (Fig. 3c and Fig. S5 and S7, Table S3, ESI†). In their powder state, they exhibit relatively strong fluorescence as well. Besides, red-shifted fluorescence emissions were observed with maxima centered at 662, 620, 653 and 644 nm, respectively, for **1a–d** (Fig. 3b) and their fluorescence quantum yields range from 0.13 to 0.25 as summarized in Table S3 (ESI†). The bright solid-state red-emissive properties are similar to those in a recent paper published by Niu and co-workers.[15f] **1a–c** exhibit characteristic J-aggregating packing as previously reported.[14b,16a] Their packing patterns are observed to adopt a coplanar inclined arrangement of the transition dipoles, respectively, with slip angles of 23.2°, 30.7°, and 18.5°, and adjacent interlayer distances of 4.12 Å, 3.38 Å, and 3.88 Å for **1a–c** (Fig. S1–S3, ESI†). The head-to-head or head-to-tail dimer and J-aggregating crystal packing might inhibit the free rotation of the *meso*-2-ketopyrrolyl group, reduce the nonradiative rate of energy loss, and further enhance their solid-state red emissive quantum yields.

To further understand the electronic properties of the *meso*-2-ketopyrrolyl BODIPYs, the density functional theory (DFT) and time-dependent DFT (TDDFT) calculations were performed using a B3LYP/6-311++G* basis set. As can be deduced from Fig. 4, the HOMO−1 electronic distribution of **1a** is mainly localized on the 2-ketopyrrolyl group segment, while the LUMO is delocalized over the BODIPY core, indicating an obvious ICT character. The TDDFT calculated parameter (Table S4, ESI†) of BODIPY **1a** shows $S_0 \rightarrow S_1$ with an excitation wavelength of

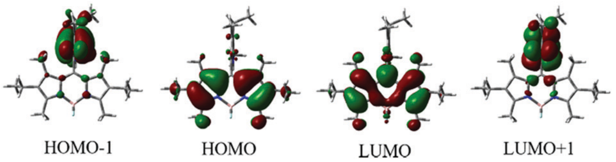

Fig. 4 Molecular frontier orbital plots of *meso*-2-ketopyrrolyl BODIPY **1a** calculated with DFT at the B3LYP/6-31+G(d,p) level.

468 nm, oscillator strength f = 0.2725; and $S_0 \rightarrow S_2$ with an excitation wavelength of 449 nm, oscillator strength f = 0.3296. These two excited states may all contribute to the maximum absorption. The $S_0 \rightarrow S_1$ energy state is fully contributed by HOMO−1 → LUMO and HOMO → LUMO (Table S4, ESI†).

2.4 AIE studies

Encouraged by their photophysical properties as observed above, we studied their AIE behaviour by gradually increasing the water fraction from 0 to 99% in the acetonitrile–water system and measuring the variation of their absorption and fluorescence emission. With an increasing water content of over 80%, their absorption spectra exhibited more broad and dual peaks (Fig. S10a, S11a, S12a and S13a, ESI†), which are characteristic of the J-type packing[14b,16a] and possibly formed nanoparticles. As shown in Fig. 3d and Fig. S10b (ESI†), **1a** exhibits relatively weak emission in pure acetonitrile. However, by increasing the water fraction to 90%, its fluorescence intensity increases instantaneously with the redshifted emission maximum at 591 nm, indicating that **1a** is a new AIEgen. Similarly, **1b–d** also exhibited excellent AIE-activity in the aforesaid solvent system (Fig. S11b, S12b and S13b, ESI†). It is worth mentioning that a further increase of the water fraction up to 99% for **1b** and **1c** (Fig. S11b and S12b, ESI†) leads to an increase of the fluorescence intensity, while maintaining the position of their emission maxima. Their red-shifted and enhanced emissions in the aggregated state might be ascribed to their rigidified molecular structures as well as strong dipole–dipole interactions. Their fluorescence activities above revealed that they exhibit notable AIE-activity. The AIE phenomenon[16–20] is very unusual for the members of the BODIPY family which normally exhibit a very strong tendency of ACQ. To our best knowledge, only very limited AIE-active BODIPYs have been reported.[16–18] Some of them were elegantly designed through conjugation of BODIPY derivatives with AIE-active tetraphenylethene moieties developed by Tang.[17]

To make clear their aggregation behaviours, **1a–d** with a water fraction of 90% in the acetonitrile–water system were, respectively, subjected to scanning electron microscopy (SEM) and transmission electron microscopy (TEM). Very interestingly, different types of nanoaggregates were formed within their solutions. As shown in Fig. 5a and Fig. S14a and b (ESI†), nanoball aggregates of relatively uniform size were created for **1a**, **1c** and **1d**, respectively. In sharp contrast to them, **1b** gave cuboid nanoaggregates about 200 nm wide (Fig. 5b). The shape and size of these aggregates are further confirmed by the corresponding TEM plots (Fig. 5c and d and Fig. S14c and d, ESI†), which are in good agreement with SEM. Dynamic light scattering (DLS) measurements of **1a** and **1b** with the water fraction equal to 99% in the acetonitrile–water system (Fig. S15 and S16, ESI†) revealed the average diameter sizes of 200 and 348 nm and the corresponding PDI values of 0.098 and 0.283, respectively. Among the formed nanoaggregates, the size of the aggregates of **1a** is smaller, which may be ascribed to its greater hydrophobicity due to its possession of more alkyl substituents. The obviously morphological distinction between nanoballs for **1a** and nanocuboids for **1b** indicates that their aggregate morphologies could be tunable. The observed phenomenon was similar to AIE luminogens based on quinoline-BODIPYs developed by Pandey.[18a]

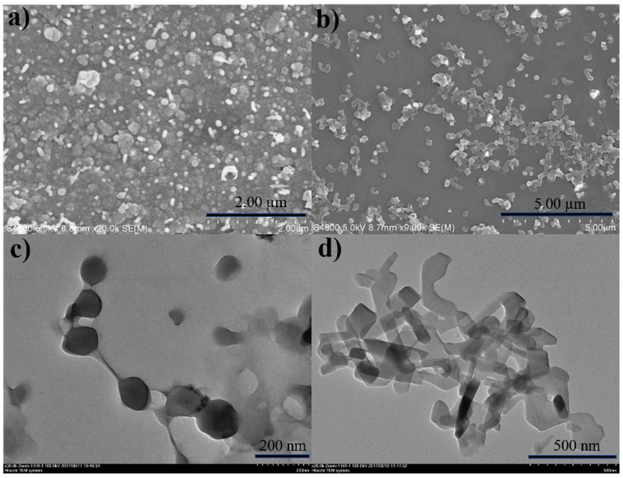

Fig. 5 SEM (a and b) and TEM (c and d) images of nanoballs for **1a** (50 μM) and nanocuboids for **1b** (30 μM) in the acetonitrile–water system containing a water fraction equal to 90%. The insets show the corresponding magnified images.

2.5 Viscosity studies

To decrease the rapid non-radiative decay and restrict their rotations, we tested viscosity (η) sensitivity for these two novel *meso*-2-ketopyrrolyl BODIPYs as FMRs by increasing the volume ratio of glycerol to methanol. The gradually increased viscosity restricts the motions of the *meso*-2-ketopyrrolyl groups, decreases their nonradiative rate of energy loss, and naturally enhances their fluorescence for **1a–d** (Fig. 6a and Fig. S17–S19, ESI†). The gradual increase of the viscosity from 0.6 to 360 cP brings a continuous enhancement of the fluorescence emission intensity (F) of **1a** and **1b** at 560 and 530 nm, respectively (Fig. 6a and Fig. S17, ESI†). More importantly, we were fortunate to find that both dyes exhibited quite perfect linear relationships between their $\log(F/F')$ and $\log\eta$ (Pearson's r = 0.996 for **1a**, Fig. 6b; and Pearson's r = 0.990 for **1b**, Fig. S20, ESI†). In comparison with that of the fluorescence intensity, the detection of the fluorescence lifetime has more intrinsic advantages for practical applications in imaging, because the fluorescence lifetime is independent of the sample concentration and does not depend on the intensity of the laser.[6–8] Thus, the fluorescence decays of these *meso*-2-ketopyrrolyl BODIPYs **1a** and **1b** in methanol/glycerol mixtures with different viscosities were studied (Fig. 6c and Fig. S21, ESI†). Similar to that observed in the increase of the

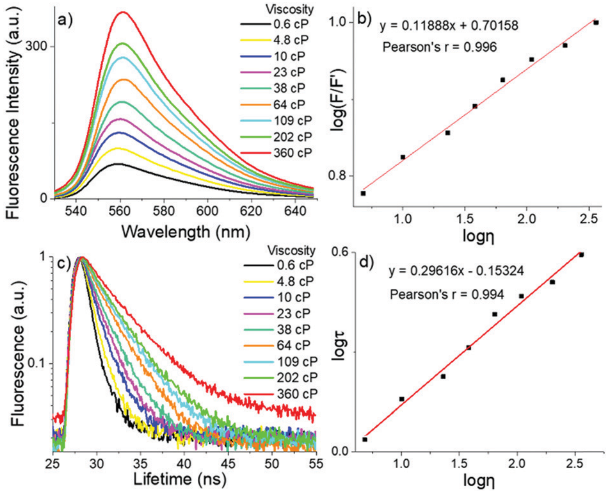

Fig. 6 (a) Fluorescence intensity of **1a** (5 μM, excited at 500 nm) with the variation of the viscosity of the system in the methanol–glycerol system. (b) Linear working curve between log(F/F') and log η of **1a** (560 nm). (c) Fluorescence lifetime for **1a** with the variation of the viscosity collected at 560 nm. (d) Linear working curve between log τ and log η for **1a**.

fluorescence intensity of **1a**, a remarkable increase of the fluorescence lifetime (τ) at 560 nm (from 0.8 ns to 3.9 ns) was observed for **1a** with the increase of the viscosity from 0.6 cP to 360 cP in methanol/glycerol solutions. In particular, a greatly perfect linear relationship was also observed between log τ and log η with Pearson's r of 0.994 (Fig. 6d), indicating that *meso*-2-ketopyrrolyl BODIPY **1a** we have developed in this contribution could be used to construct calibration curves to quantitatively detect viscosity *in vitro*. Similar linear correlations of the fluorescence lifetimes (Fig. S22, ESI†) for **1b** were also determined as a function of viscosity with Pearson's r of 0.997, respectively, indicating that **1b** might also be used as a viscosity mapping rotor for real-time tracking viscosity changes during cell apoptosis events.

2.6 Cell culture

Before they were used for MTT and cellular uptake, the morphology of **1a** (5 μM) was studied in phosphate-buffered saline (PBS, pH = 7.4). In distinct contrast to those at a concentration of 50 μM, no nanoparticles were observed for 5 μM **1a** (Fig. S23a, ESI†). As confirmed by energy dispersive X-ray spectrometer (EDS, Fig. S23, ESI†) mapping, **1a** was found to be dispersed in PBS. Besides, the solubility of **1a** (5 μM) was studied in Dulbecco's modified Eagle's medium (DMEM). As shown in Fig. S24 (ESI†), **1a** in DMEM exhibits similar absorbances at different concentrations with the absorption wavelength maximum of 540 nm, and the absorbance complies with the Lambert–Beer law, with lg $\varepsilon_{\mathrm{abs}}$ of 4.61. The results indicated that aggregates were not formed for 5 μM **1a** in DMEM. The results further confirmed that these dyes were not in the aggregated-form when used for cellular uptake, and intracellular micro-viscosity might play a critical role. Membrane permeation is the most likely way for small molecule fluorescent dyes to enter the cells. To make clear if our dyes could localize subcellular organelles, the co-localization experiments were carried out. The co-localization imaging studies (Fig. S25 and S26, ESI†) show that the positions of different subcellular organelles with different viscosities (like cytoplasm, lysosome and the ER) are all distributed for **1a** and **1b**. It is precisely because these dyes are dispersed in the cytoplasm, so they can be used to detect the overall level of intracytoplasmic viscosity.

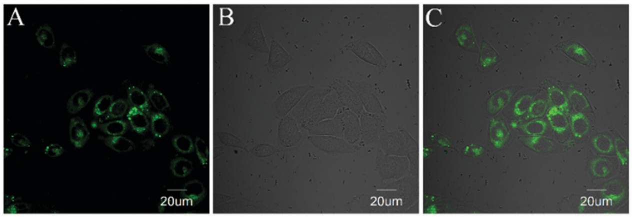

Fig. 7 Imaging of **1a** in MCF-7 cells. (A) MCF-7 cells stained with **1a** (5 μM, λ_{ex} = 515 nm, λ_{em} = 520–600 nm); (B) DIC image; and (C) merge of A and B.

Inspired by the excellent viscosity sensitivity above for these novel *meso*-2-ketopyrrolyl BODIPYs, we then studied their cell imaging. After incubation with **1a** and **1b** for only 10 minutes (Fig. 7 and Fig. S27, ESI†), their green fluorescence was observed in the cytoplasm of MCF-7. Both **1a** and **1b** quickly entered cells and exhibited unexpectedly biocompatible capability. MTT assay as a standard cell viability protocol was then used to study their cytotoxic effects on MCF-7 cells (Fig. S28 and S29, ESI†). A high cell viability was observed with a survival rate of above 85% (in 1.0 × 10^4 cells per well) after treating MCF-7 cells with dye **1a** or **1b** (0–10 μM) for 24 h. This low cytotoxicity makes these novel dyes applicable for *in vitro* intracellular imaging.

2.7 Viscosity determination in real-time during apoptosis

Considering the perfect correlation of the fluorescence lifetimes of these *meso*-2-ketopyrrolyl BODIPYs with the viscosity of media, we further investigated the performance of **1a** and **1b** as FMRs in monitoring the viscosity changes during the pathological processes such as cell apoptosis events. Therefore, etoposide, a clinical antitumor drug that induces cell apoptosis by inhibiting the repair of damaged DNA, was used to stimulate MCF-7 cells. The FLIM image of these cells revealed that the fluorescence lifetime of **1a** in cytoplasm changed from 2.45 ns to 3.8 ns during the 60 minutes of etoposide treatment (Fig. 8 and Fig. S30, ESI†). The average viscosity of the cytoplasm around **1a** significantly

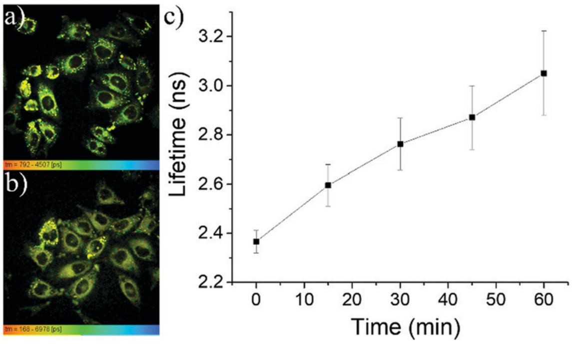

Fig. 8 (a and b) FLIM images of MCF-7 cells incubated with etoposide for 0 and 45 min, respectively. (c) Variation of the fluorescence lifetimes of **1a** with the extension of the cell apoptosis time.

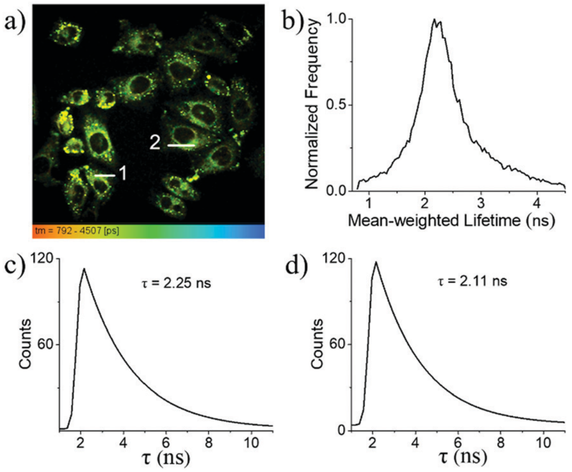

Fig. 9 (a) Intracellular FLIM of **1a** (MCF-7 cells, the mean-weighted lifetime range is 0.80–4.50 ns). (b) Histogram showing the fluorescence lifetime distribution (*x* axis: the lifetime and *y* axis: normalized fequency of the black cross point). (c) and (d) Fluorescence lifetimes of regions 1 (c) and 2 (d) marked in (a).

increased from 70 cP to 300 cP and a quite similar linear lifetime–viscosity relationship during cell apoptosis (Fig. 8c) was obtained. The linear correlation of **1b** (Fig. S31, ESI†) seems to be slightly lost. This might be ascribed to the relatively weak lipotropism and poor solubility compared to those of **1a**.

In combination with FLIM, **1a** is a reliable tool for the determination of the local intracellular viscosity. As shown in the FLIM images of MCF-7 cells (Fig. 9a), the fluorescence lifetime of **1a** within cells can be clearly mapped from its fluorescence lifetime distribution histogram. For example, the average fluorescence lifetime was established to be 2.4 ns for **1a** (Fig. 9b). This indicates that inside cytoplasm, the average viscosity around **1a** is about 60 cP as shown in the calibration graph (Fig. 6d). The high spatial resolution of these FLIM images was found to be compatible with their corresponding confocal images. This makes it feasible to indicate the local viscosities in different areas of cytoplasm based on the determination of their fluorescence lifetimes. For example, within different randomly chosen intracellular regions, the precision of the resultant fluorescence decay curves is almost identical to those obtained in the solution state. As shown in Fig. 9c and d, the different regions (Fig. 9a) of cells have different lifetimes of 2.25 ns and 2.11 ns, with respect to 50.9 and 41.0 cP, respectively, indicating that the change in intracellular viscosity could be facilely detected by our *meso*-2-ketopyrrolyl derived BODIPY **1a**.

3. Conclusions

In summary, we have first synthesized a novel family of unconventional *meso*-2-ketopyrrolyl BODIPYs *via* the efficient condensation reactions between oxalyl chloride and substituted pyrrolic derivatives. The *meso*-2-ketopyrrolyl BODIPYs exhibited high red fluorescence quantum yields of up to 25% from 620 to 661 nm, and notable AIE-active and viscosity-sensitive characteristics. The formed nanoaggregates were observed to exhibit morphological distinctions with average diameters owing to different substituents. In addition, the restriction of the rotation of the *meso*-ketopyrrolyl group in viscous media resulted in large fluorescence enhancement and lengthened the fluorescence lifetime from 0.8 to 3.9 ns, which are in good correlation with the variation of the viscosity in the media. More importantly, as novel mapping viscosity BODIPY indicators, they show excellent applicability for real-time tracking viscosity changes during cell apoptosis events, and for monitoring normal and abnormal cell viscosities and for further quantifying the local viscosity within the living cell. This easy strategy and a perfect linear relationship between the fluorescence lifetime and viscosity might indicate that the developed *meso*-2-ketopyrrolyl derived BODIPYs here are suitable viscosimeters as designed.

4. Experimental

General methods

Reagents and solvents were used as received from commercial suppliers unless noted otherwise. All reactions were performed in oven-dried or flame-dried glassware, and monitored by TLC using 0.25 mm silica gel plates with a UV indicator. ^{1}H and ^{13}C NMR were recorded on a 300 MHz NMR spectrometer at room temperature. Chemical shifts (δ) are given relative to $CDCl_3$ (7.26 ppm for ^{1}H and 77 ppm for ^{13}C) or internal tetramethylsilane (abbreviated as TMS). High-resolution mass spectra (HRMS) were obtained using APCI-TOF in a positive mode.

Syntheses of *meso*-2-ketopyrrolyl BODIPYs 1a and b

Synthesis of 1a. 3-Ethyl-2,4-methylpyrrole (0.95 mL, 7 mmol) was dissolved into 60 mL freshly distilled 1,2-dichloroethane under argon. To this solution was dropwise added oxalyl chloride (0.17 mL, 2 mmol) in 1,2-dichloroethane (10 mL) *via* a pressure-equalizing dropping funnel under ice-bath conditions. By increasing the reaction temperature to 35 °C, the reaction mixture was then allowed to stir at this temperature for 3 h. To this reaction mixture was added Et_3N (2 mL) under ice-bath conditions. The mixture was further stirred for 10 minutes before subsequent addition of $BF_3{\cdot}OEt_2$ (3 mL) at this temperature *via* a syringe. The reaction mixture was left stirring overnight under refluxing conditions. The reaction mixture was cooled down to room temperature, poured into water (150 mL) and extracted with dichloromethane (3 × 40 mL). Organic layers were combined, and subsequently washed with water. The resultant organic layers were dried over anhydrous sodium sulfate and filtered, and the solvent was evaporated under vacuum. The crude product was then purified by silica gel chromatography (petroleum/ethyl acetate = 4/1, v/v). Target **1a** was obtained as a reddish powder in 18% yield (163 mg). ^{1}H NMR (300 MHz, $CDCl_3$) δ: 9.49 (brs, 1H; NH), 2.52 (s, 6H; CH_3), 2.36–2.28 (m, 9H; CH_2, CH_3), 1.86 (s, 9H; CH_3), 1.00 (t, J = 7.2 Hz, 9H; CH_3). ^{13}C NMR (75 MHz, $CDCl_3$) δ: 179.2, 154.8, 136.9, 136.7, 136.3, 132.7, 130.5, 128.4, 128.2, 126.1, 17.1, 15.2, 14.7, 12.7, 11.9, 11.1, 11.0, 10.6. HRMS (APCI): m/z = 454.2831 $[M + H]^+$.

Synthesis of 1b. As described in the procedure for **1a** above, BODIPY **1b** was prepared as a reddish powder in 23% yield

(169 mg) from 2,4-methylpyrrole (0.73 mL, 7 mmol) and oxalyl chloride (0.17 mL, 2 mmol). ^{1}H NMR (300 MHz, $CDCl_3$) δ: 9.39 (brs, 1H; NH), 6.01 (s, 2H), 5.84 (s, 1H), 2.54 (s, 6H; CH_3), 2.32 (s, 3H; CH_3), 1.95 (s, 6H; CH_3), 1.93 (s, 3H; CH_3). ^{13}C NMR (75 MHz, $CDCl_3$) δ: 178.9, 156.8, 141.6, 138.7, 137.8, 133.3, 129.1, 128.7, 121.0, 113.8, 14.8, 13.6, 13.4, 13.0. HRMS (APCI): m/z = 370.1907 $[M + H]^+$.

General synthetic procedure for 1a–d

To a dried flask containing dipyrrolediketone **2** (1 mmol) in dichloromethane (60 mL) was added 0.2 mL $BF_3{\cdot}OEt_2$. The solution turned brown quickly. Then 2,4-dimethylpyrrole or 2,4-dimethyl-3-ethylpyrrole (1.2 mmol, 1.2 equivalents) in 10 mL dichloromethane was dropwise added slowly. The mixture was stirred for 3 hours at room temperature (35 °C). When dipyrrolediketone **2** was consumed completely, 3 mL of Et_3N was added and the mixture was stirred for 10 minutes before subsequent addition of $BF_3{\cdot}OEt_2$ (3.5 mL) through a syringe. The reaction mixture was left stirring for 30 min. Then the reaction mixture was extracted with EtOAc (30 mL × 3). The organic layers were combined, dried over anhydrous Na_2SO_4, filtered, and evaporated to dryness under vacuum. The crude product was purified by column chromatography on silica gel (hexane/EtOAc = 4/1, v/v) and was further recrystallized from hexane to give **1a–d** as reddish powders.

1a. It was prepared using the above procedure from **2a** (240 mg, 0.8 mmol) and 2,4-dimethyl-3-ethylpyrrole (1.2 eq.), affording a reddish powder in 45% yield (164 mg). ^{1}H NMR (300 MHz, $CDCl_3$) δ: 9.49 (brs, 1H; NH), 2.52 (s, 6H; CH_3), 2.36–2.28 (m, 9H; CH_2, CH_3), 1.86 (s, 9H; CH_3), 1.00 (t, J = 7.2 Hz, 9H; CH_3). ^{13}C NMR (75 MHz, $CDCl_3$) δ: 179.2, 154.8, 136.9, 136.7, 136.3, 132.7, 130.5, 128.4, 128.2, 126.1, 17.1, 15.2, 14.7, 12.7, 11.9, 11.1, 11.0, 10.6. HRMS (APCI): m/z = 454.2831 $[M + H]^+$.

1b. It was prepared using the above procedure from **2b** (195 mg, 0.8 mmol) and 2,4-dimethylpyrrole (1.2 eq.), affording a reddish powder in 32% yield (94 mg). ^{1}H NMR (300 MHz, $CDCl_3$) δ: 9.39 (brs, 1H; NH), 6.01 (s, 2H), 5.84 (s, 1H), 2.54 (s, 6H; CH_3), 2.32 (s, 3H; CH_3), 1.95 (s, 6H; CH_3), 1.93 (s, 3H; CH_3). ^{13}C NMR (75 MHz, $CDCl_3$) δ: 178.9, 156.8, 141.6, 138.7, 137.8, 133.3, 129.1, 128.7, 121.0, 113.8, 14.8, 13.6, 13.4, 13.0. HRMS (APCI): m/z = 370.1907 $[M + H]^+$.

1c. It was prepared using the above procedure from **2a** (240 mg, 0.8 mmol) and 2,4-dimethylpyrrole (1.2 eq.), affording a reddish powder in 45% yield (153 mg). ^{1}H NMR (300 MHz, $CDCl_3$) δ: 9.36 (s, 1H), 5.96 (s, 1H), 2.53 (s, 6H), 2.32–2.35 (m, 4H), 2.28 (s, 3H), 1.92 (s, 3H), 1.88 (s, 3H), 1.88 (s, 3H), 0.98–1.03 (m, 6H). ^{13}C NMR (75 MHz, $CDCl_3$) δ: 178.6, 156.7, 154.9, 140.4, 137.9, 137.5, 136.9, 133.5, 130.6, 129.0, 128.6, 128.0, 126.2, 120.2, 17.1, 16.9, 15.2, 14.6, 13.6, 12.9, 11.9, 11.1, 10.6. HRMS (APCI): m/z = 426.2522 $[M + H]^+$.

1d. It was prepared using the above procedure from **2b** (195 mg, 0.8 mmol) and 2,4-dimethyl-3-ethylpyrrole (1.2 eq.), affording a reddish powder in 41% yield (130 mg). ^{1}H NMR (300 MHz, $CDCl_3$) δ: 9.76 (s, 1H), 5.96 (s, 1H), 5.84 (s, 1H), 2.53 (s, 6H), 2.32 (s, 5H), 1.93 (s, 6H), 1.89 (s, 3H), 1.00 (s, 3H). ^{13}C NMR (75 MHz, $CDCl_3$) δ: 179.2, 156.8, 155.0, 140.3, 139.7, 137.7, 137.1, 133.7, 133.6, 129.0, 128.8, 120.3, 113.8, 113.6, 17.1, 14.6, 13.5, 13.4, 13.2, 12.9, 11.0. HRMS (APCI): m/z = 398.2208 $[M + H]^+$.

Photophysical characterization

UV-visible absorption and fluorescence emission spectra were recorded on commercial spectrophotometers (190–870 nm scan range, Shimadzu UV-2450 and Hitachi F-4500) at room temperature (1 cm quartz cuvette). The absolute fluorescence quantum efficiencies in different organic solvents (excited at 500 nm for **1a**, excited at 480 nm for **1b–d**) and the powder state (excited at 550 nm for **1a** and 500 nm for **1b–d**) of the *meso*-2-ketopyrrolyl derived BODIPYs **1a–d** were obtained using an Edinburgh FLS 920 fluorescence spectrometer by comparing the areas under the corrected emission spectrum of the test sample using an integrating sphere according to the definition of fluorescence efficiency,[21] using eqn (1) given below:

$$\Phi_F = \frac{N_{em}}{N_{abs}} = \frac{\alpha\int\frac{\lambda}{hc}I_{em}(\lambda)d\lambda}{\alpha\int\frac{\lambda}{hc}[I_{ex}(\lambda) - I_{ex}{}'(\lambda)]d\lambda} \qquad (1)$$

where N_{em} and N_{abs} are the numbers of emitted and absorbed photons, respectively, α is the calibration factor for the measurement setup, λ is the wavelength, h is Planck's constant, c is the speed of light, $I_{em}(\lambda)$ is the emission intensity at λ, and $I_{ex}(\lambda)$ and $I_{ex}{}'(\lambda)$ are the intensities of the excitation laser beam with λ in the absence and presence of the sample, respectively. The measured Φ_F value is independent of the shape and thickness of the sample and the power of the excitation laser.

The fluorescence lifetime (τ) was measured by a time-correlated single photon counting method using an Edinburgh FLS 980 fluorescence spectrometer and emission was monitored at the peak maximum (excited at 470 nm). The fluorescence lifetime values were obtained from deconvolution and distribution lifetime analysis. The solvents were obtained by mixing methanol and glycerol in different proportions. The viscosity values were referenced to previously reported articles.[10]

Crystals suitable for X-ray crystallographic analysis

CCDC 1541729 (**1a**), CCDC 1541728 (**1b**) and CCDC 1901461 (**1c**)† contain the supplementary crystallographic data for this paper. Diffraction data were collected using a Bruker APEXII CCD area detector diffractometer using graphite-monochromated Mo-Kα radiation (λ = 0.71073 Å) at 293(2) K, with ϕ and ω scan techniques. An empirical absorption correction was applied with the SADABS program. Using Olex2[22a] or SHELXL-97,[22b] the structure was solved with the ShelXT[23] structure solution program using direct methods and refined with the ShelXL[24] refinement package using least squares minimisation. The hydrogen atom coordinates were calculated with SHELXL by using an appropriate riding model with varied thermal parameters. The residual electron densities were of no chemical significance.

DFT computations

The ground state geometry was optimized by using the DFT method at the B3LYP/6-31+G(d,p) level. The same method was used for vibrational analysis to verify that the optimized structures correspond to local minima on the energy surface. TD-DFT computations were used to obtain the vertical excitation energies and oscillator strengths for the optimized ground state equilibrium geometries at the B3LYP/6-31+G(d, p) theoretical level. TD-DFT calculations of **1a** in dichloromethane were done using the Self-Consistent Reaction Field method and Polarizable Continuum Model.

Cell culture

MCF-7 cells were obtained from the Institute of Basic Medical Sciences (IBMS) of the Chinese Academy of Medical Sciences (CAMS). All cell lines were maintained under standard culture conditions (an atmosphere of 5% CO_2 and 95% air at 37 °C) in DMEM, supplemented with 10% FBS (fetal bovine serum). The cells were used in the exponential phase of growth on 35 mm glass bottom culture dishes for 24 h. The cells were treated with 5 μM of **1a** and **1b** in culture media for 10 min at 37 °C with 5% CO_2 in a humidified incubator. Fluorescence imaging was then carried out after washing the cells with PBS. For the control experiment, the cells without treatment of dyes did not show any noticeable fluorescence under the same conditions.

Cytotoxicity study

MCF-7 cells (10^6 cells mL^{-1}) were dispersed within replicate 96-well microtiter plates to a total volume of 200 μL $well^{-1}$. Plates were maintained at 37 °C in a 5% CO_2 and 95% air incubator for 4–6 h. Then MCF-7 cells were incubated for 24 h with different concentrations of **1a** and **1b**. MTT solution was then added to each well. After 4 h, the remaining MTT solution was removed, and 150 μL of DMSO was added to each well to dissolve formazan crystals. Absorbance was measured at 490 nm in a Triturus microplate reader.

Viscosity determination in real-time during apoptosis

The fluorescence lifetimes of **1a** under different conditions were obtained with an excitation wavelength of 515 nm and collected at 520–600 nm. The fluorescence lifetimes of **1b** under different conditions were obtained with an excitation wavelength of 488 nm and collected at 510–600 nm. MCF-7 cells internalized with **1a** and **1b** were washed with PBS and then etoposide was added.[11] Fluorescence images were obtained at different time points: 0, 5, 15, 30, 45, and 60 min.

Conflicts of interest

There are no conflicts to declare.

Acknowledgements

This work was supported by the National Natural Science Foundation of China (Grant No. 21672006, 21672007, 21402001 and 21871006), Hong Kong Polytechnic University (1-YW2T and 1-ZE1C), the Hong Kong Research Grants Council (C6009-17G), the Open Funds of Nanjing University State Key Laboratory of Coordination Chemistry (SKLCC1911), and the Doctoral up Starting Foundation of Anhui Normal University (2017XJJ28).

References

1 (*a*) S. J. Singer and G. L. Nicolson, *Science*, 1972, **175**, 720–731; (*b*) S. Chen, Y. Hong, Y. Zeng, Q. Sun, Y. Liu, E. Zhao, G. Bai, J. Qu, J. Hao and B. Z. Tang, *Chem. – Eur. J.*, 2015, **21**, 4315–4320; (*c*) P. Ning, P. Dong, Q. Geng, L. Bai, X. Tian, R. Shao, L. Li and X. Meng, *J. Mater. Chem. B*, 2017, **5**, 2743–2749; (*d*) Y. He, J. Shin, W. Gong, P. Das, J. Qu, Z. Yang, W. Liu, C. Kang, J. Qu and J. S. Kim, *Chem. Commun.*, 2019, **55**, 2453–2456.

2 (*a*) M. K. Kuimova, S. W. Botchway, A. W. Parker, M. Balaz, H. A. Collins, H. L. Anderson, K. Suhling and P. R. Ogilby, *Nat. Chem.*, 2009, **1**, 69–73; (*b*) M. K. Kuimova, *Phys. Chem. Chem. Phys.*, 2012, **14**, 12671–12686; (*c*) X. Qian and Z. Xu, *Chem. Soc. Rev.*, 2015, **44**, 4487–4493; (*d*) F. Liu, T. Wu, J. Cao, S. Cui, Z. Yang, X. Qiang, S. Sun, F. Song, J. Fan, J. Wang and X. Peng, *Chem. – Eur. J.*, 2013, **19**, 1548–1553; (*e*) H. Doan, S. L. Raut, D. Yale, M. Balaz, S. V. Dzyuba and Z. Gryczynski, *Chem. Commun.*, 2016, **52**, 9510–9513; (*f*) W. Chen, C. Gao, X. Liu, F. Liu, F. Wang, L. Tang and J.-H. Jiang, *Anal. Chem.*, 2018, **90**, 8736–8741.

3 (*a*) M. R. Dent, I. Lopez-Duarte, C. J. Dickson, P. Chairatana, H. L. Anderson, I. R. Gould, D. Wylie, A. Vyšniauskas, N. J. Brooks and M. K. Kuimova, *Chem. Commun.*, 2016, **52**, 13269–13272; (*b*) S.-C. Lee, J. Heo, J.-W. Ryu, C.-L. Lee, S. Kim, J.-S. Tae, B.-O. Rhee, S.-W. Kim and O.-P. Kwon, *Chem. Commun.*, 2016, **52**, 13695–13698; (*c*) T. Luo, Y. Lu, S. Liu, D. Lin and J. Qu, *Anal. Chem.*, 2017, **89**, 8104–8111; (*d*) M. Ren, B. Deng, K. Zhou, X. Kong, J.-Y. Wang and W. Lin, *Anal. Chem.*, 2017, **89**, 552–555; (*e*) L. Hou, P. Ning, Y. Feng, Y. Ding, L. Bai, L. Li, H. Yu and X. Meng, *Anal. Chem.*, 2018, **90**, 7122–7126.

4 (*a*) G. S. Zubenko, U. Kopp, T. Seto and L. L. Firestone, *Psychopharmacology*, 1999, **145**, 175–180; (*b*) H. Tan, Y. Qiu, H. Sun, J. Yan and L. Zhang, *Chem. Commun.*, 2019, **55**, 2688–2691.

5 (*a*) A. Loudet and K. Burgess, *Chem. Rev.*, 2007, **107**, 4891–4932; (*b*) G. Ulrich, R. Ziessel and A. Harriman, *Angew. Chem., Int. Ed.*, 2008, **47**, 1184–1201; (*c*) N. Boens, V. Leen and W. Dehaen, *Chem. Soc. Rev.*, 2012, **41**, 1130–1172; (*d*) H. Lu, J. Mack, Y. Yang and Z. Shen, *Chem. Soc. Rev.*, 2014, **43**, 4778–4823; (*e*) Y. Ni and J. Wu, *Org. Biomol. Chem.*, 2014, **12**, 3774–3791; (*f*) N. Boens, B. Verbelen and W. Dehaen, *Eur. J. Org. Chem.*, 2015, 6577–6595.

6 (*a*) M. K. Kuimova, G. Yahioglu, J. A. Levitt and K. Suhling, *J. Am. Chem. Soc.*, 2008, **130**, 6672–6673; (*b*) N. A. Hosny, G. Mohamedi, P. Rademeyer, J. Owen, Y. L. Wu, M. X. Tang, R. J. Eckersley, E. Stride and M. K. Kuimova, *Proc. Natl. Acad. Sci. U. S. A.*, 2013, **110**, 9225–9230; (*c*) I. López-Duarte, T. T. Vu, M. A. Izquierdo, J. A. Bull and M. K. Kuimova, *Chem. Commun.*, 2014, **50**, 5282–5284; (*d*) A. Vyšniauskas, M. Qurashi, N. Gallop, M. Balaz, H. L. Andersonb and M. K. Kuimova, *Chem. Sci.*, 2015, **6**, 5773–5778; (*e*) T. T. Vu,

R. Méallet-Renaul, G. Clavier, B. A. Trofimov and M. K. Kuimova, *J. Mater. Chem. C*, 2016, **4**, 2828–2833; (*f*) P. S. Sherin, I. López-Duarte, M. R. Dent, M. Kubánková, A. Vyšniauskas, J. A. Bull, E. S. Reshetnikova, A. S. Klymchenko, Y. P. Tsentalovich and M. K. Kuimova, *Chem. Sci.*, 2017, **8**, 3523–3528; (*g*) J. E. Chambers, M. Kubánková, R. G. Huber, I. López-Duarte, E. Avezov, P. J. Bond, S. J. Marciniak and M. K. Kuimova, *ACS Nano*, 2018, **12**, 4398–4407.

7 (*a*) M. A. H. Alamiry, A. C. Benniston, G. Copley, K. J. Elliott, A. Harriman, B. Stewart and Y.-G. Zhi, *Chem. Mater.*, 2008, **20**, 4024–4032; (*b*) S. Raut, J. Kimball, R. Fudala, H. Doan, B. Maliwal, N. Sabnis, A. Lacko, I. Gryczynski, S. V. Dzyuba and Z. Gryczynski, *Phys. Chem. Chem. Phys.*, 2014, **16**, 27037–27042; (*c*) S. L. Raut, J. D. Kimball, R. Fudala, I. Bora, R. Chib, H. Jaafari, M. K. Castillo, N. W. Smith, I. Gryczynski, S. V. Dzyuba and Z. Gryczynski, *Phys. Chem. Chem. Phys.*, 2016, **18**, 4535–4540; (*d*) L.-L. Li, K. Li, M.-Y. Li, L. Shi, Y.-H. Liu, H. Zhang, S.-L. Pan, N. Wang, Q. Zhou and X.-Q. Yu, *Anal. Chem.*, 2018, **90**, 5873–5878.

8 (*a*) Z. Yang, Y. He, J.-H. Lee, N. Park, M. Suh, W.-S. Chae, J. Cao, X. Peng, H. Jung, C. Kang and J. S. Kim, *J. Am. Chem. Soc.*, 2013, **135**, 9181–9185; (*b*) Z. Yang, Y. He, J. H. Lee, W.-S. Chae, W. X. Ren, J. H. Lee, C. Kang and J. S. Kim, *Chem. Commun.*, 2014, **50**, 11672–11675; (*c*) H. Lee, Z. Yang, Y. Wi, T. W. Kim, P. Verwilst, Y. H. Lee, G. Han, C. Kang and J. S. Kim, *Bioconjugate Chem.*, 2015, **26**, 2474–2480; (*d*) D. Dziuba, P. Jurkiewicz, M. Cebecauer, M. Hof and M. Hocek, *Angew. Chem., Int. Ed.*, 2016, **55**, 174–178; (*e*) W. Zhang, W. Sheng, C. Yu, Y. Wei, H. Wang, E. Hao and L. Jiao, *Chem. Commun.*, 2017, **53**, 5318–5321.

9 (*a*) H. L. Kee, C. Kirmaier, L. Yu, P. Thamyongkit, W. J. Youngblood, M. E. Calder, L. Ramos, B. C. Noll, D. F. Bocian, W. R. Scheidt, R. R. Birge, J. S. Lindsey and D. Holten, *J. Phys. Chem. B*, 2005, **109**, 20433–20443; (*b*) E. Bahaidarah, A. Harriman, P. Stachelek, S. Rihn, E. Heyer and R. Ziessel, *Photochem. Photobiol. Sci.*, 2014, **13**, 1397–1401.

10 L. Wang, Y. Xiao, W. Tian and L. Deng, *J. Am. Chem. Soc.*, 2013, **135**, 2903–2906.

11 H. Zhu, J. Fan, M. Li, J. Cao, J. Wang and X. Peng, *Chem. – Eur. J.*, 2014, **20**, 4691–4696.

12 R. Guliyev, S. Ozturk, E. Sahin and E. U. Akkaya, *Org. Lett.*, 2012, **14**, 1528–1531.

13 C. Yu, E. Hao, T. Li, J. Wang, W. Sheng, Y. Wei, X. Mu and L. Jiao, *Dalton Trans.*, 2015, **44**, 13897–13905.

14 (*a*) Y. Ni, L. Zeng, N.-Y. Kang, K.-W. Huang, L. Wang, Z. Zeng, Y.-T. Chang and J. Wu, *Chem. – Eur. J.*, 2014, **20**, 2301–2310; (*b*) S. Kim, J. Bouffard and Y. Kim, *Chem. – Eur. J.*, 2015, **21**, 17459–17465; (*c*) Y. Ni, R. K. Kannadorai, S. W.-K. Yu, Y.-T. Chang and J. Wu, *Org. Biomol. Chem.*, 2017, **15**, 4531–4535; (*d*) T.-I. Kim, H. Kim, Y. Choi and Y. Kim, *Sens. Actuators, B*, 2017, **249**, 229–234; (*e*) T.-I. Kim, B. Hwang, B. Lee, J. Bae and Y. Kim, *J. Am. Chem. Soc.*, 2018, **140**, 11771–11776; (*f*) J. A. Peterson, C. Wijesooriya, E. J. Gehrmann, K. M. Mahoney, P. P. Goswami, T. R. Albright, A. Syed, A. S. Dutton, E. A. Smith and A. H. Winter, *J. Am. Chem. Soc.*, 2018, **140**, 7343–7346.

15 (*a*) N. Zhao, M. G. Vicente, F. R. Fronczek and K. M. Smith, *Chem. – Eur. J.*, 2015, **21**, 6181–6192; (*b*) N. Zhao, S. Xuan, Z. Zhou, F. R. Fronczek, K. M. Smith and M. G. H. Vicente, *J. Org. Chem.*, 2017, **82**, 9744–9750; (*c*) N. Zhao, T. M. Williams, Z. Zhou, F. R. Fronczek, M. Sibrian-Vazquez, S. D. Jois and M. G. H. Vicente, *Bioconjugate Chem.*, 2017, **28**, 1566–1579; (*d*) G. Zhang, N. Zhao, P. Bobadova-Parvanova, M. Wang, F. R. Fronczek, K. M. Smith and M. G. H. Vicente, *J. Phys. Chem. A*, 2018, **122**, 6256–6265; (*e*) D. J. LaMaster, N. E. M. Kaufman, A. S. Bruner and M. G. H. Vicente, *J. Phys. Chem. A*, 2018, **122**, 6372–6380; (*f*) C. Duan, Y. Zhou, G.-G. Shan, Y. Chen, W. Zhao, D. Yuan, L. Zeng, X. Huang and G. Niu, *J. Mater. Chem. C*, 2019, **7**, 3471–3478.

16 (*a*) S. Choi, J. Bouffard and Y. Kim, *Chem. Sci.*, 2014, **5**, 751–755; (*b*) H. Chua, Y. Ni, M. Garai, B. Zheng, K.-W. Huang, Q.-H. Xu, J. Xu and J. Wu, *Chem. – Asian J.*, 2015, **10**, 1631–1634.

17 (*a*) R. Hu, C. F. A. M. Gómez-Durán, J. W. Y. Lam, J. L. Belmonte-Vázquez, C. Deng, S. Chen, R. Ye, E. Peña-Cabrera, Y. Zhong, K. S. Wong and B. Z. Tang, *Chem. Commun.*, 2012, **48**, 10099–10101; (*b*) Z. Zhao, B. Chen, J. Geng, Z. Chang, L. Aparicio-Ixta, H. Nie, C. C. Goh, L. G. Ng, A. Qin, G. Ramos-Ortiz, B. Liu and B. Z. Tang, *Part. Part. Syst. Charact.*, 2014, **31**, 481–491; (*c*) C. F. A. Gómez-Durán, R. Hu, G. Feng, T. Li, F. Bu, M. Arseneault, B. Liu, E. Peña-Cabrera and B. Z. Tang, *ACS Appl. Mater. Interfaces*, 2015, **7**, 15168–15176; (*d*) H.-T. Feng, X. Gu, J. W. Y. Lam, Y.-S. Zheng and B. Z. Tang, *J. Mater. Chem. C*, 2018, **6**, 8934–8940.

18 (*a*) R. S. Singh, R. K. Gupta, R. P. Paitandi, M. Dubey, G. Sharma, B. Koch and D. S. Pandey, *Chem. Commun.*, 2015, **51**, 9125–9128; (*b*) H. T. Feng, J.-B. Xiong, Y.-S. Zheng, B. Pan, C. Zhang, L. Wang and Y. Xie, *Chem. Mater.*, 2015, **27**, 7812–7819; (*c*) H. Manzano, I. Esnal, T. Marqués-Matesanz, J. Bañuelos, I. López-Arbeloa, M. J. Ortiz, L. Cerdán, A. Costela, I. García-Moreno and J. L. Chiara, *Adv. Funct. Mater.*, 2016, **26**, 2756–2769; (*d*) E. Sen, K. Meral and S. Atilgan, *Chem. – Eur. J.*, 2016, **22**, 736–745.

19 (*a*) J. Mei, Y. Hong, J. W. Y. Lam, A. Qin, Y. Tang and B. Z. Tang, *Adv. Mater.*, 2014, **26**, 5429–5479; (*b*) J. Mei, N. L. Leung, R. T. Lam, J. W. Kwok and B. Z. Tang, *Chem. Rev.*, 2015, **115**, 11718–11940; (*c*) M. Chen, X. Hu, J. Liu, B. Li, N. L. C. Leung, L. Viglianti, T. S. Cheung, H. H. Y. Sung, R. T. K. Kwok, I. D. Williams, A. Qin, J. W. Y. Lam and B. Z. Tang, *Chem. Sci.*, 2018, **9**, 7829–7834; (*d*) D. Wang, H. Su, R. T. K. Kwok, X. Hu, H. Zou, Q. Luo, M. M. S. Lee, W. Xu, J. W. Y. Lam and B. Z. Tang, *Chem. Sci.*, 2018, **9**, 3685–3693.

20 (*a*) S. Gan, J. Zhou, T. A. Smith, H. Su, W. Luo, Y. Hong, Z. Zhao and B. Z. Tang, *Mater. Chem. Front.*, 2017, **1**, 2554–2558; (*b*) M. Yamaguchi, S. Ito, A. Hirose, K. Tanaka and Y. Chujo, *Mater. Chem. Front.*, 2017, **1**, 1573–1579; (*c*) J. S. Ni, H. Liu, M. Jiang, Z. Zhao, Y. Chen, R. T. K. Kwok, J. W. Y. Lam, Q. Peng and B. Z. Tang, *Mater. Chem. Front.*, 2018, **2**, 1498–1507; (*d*) F. Ren, P. Liu, Y. Gao, J. Shi, B. Tong, Z. Cai and Y. Dong, *Mater. Chem. Front.*, 2019, **3**, 57–63.

21 Y. Kawamura, H. Sasabe and C. Adachi, *Jpn. J. Appl. Phys.*, 2004, **43**, 7729–7730.

22 (*a*) O. V. Dolomanov, L. J. Bourhis, R. J. Gildea, J. A. K. Howard and H. Puschmann, *J. Appl. Crystallogr.*, 2009, **42**, 339–341; (*b*) G. M. Sheldrick, *SHELXTL 5.10 for Windows NT: Structure Determination Software Programs*, Bruker Analytical X-ray Systems, Inc., Madison, WI, 1997.

23 G. M. Sheldrick, *Acta Crystallogr., Sect. A: Found. Adv.*, 2015, **71**, 3–8.

24 G. M. Sheldrick, *Acta Crystallogr., Sect. A: Found. Crystallogr.*, 2008, **64**, 112–122.